

# Super-resolution GANs of randomly-seeded fields

Alejandro Güemes

*Aerospace Engineering Research Group, Universidad Carlos III de Madrid, Leganés, Spain*

Carlos Sanmiguel Vila

*Sub-Directorate General of Terrestrial Systems, Spanish National Institute for Aerospace Technology (INTA), San Martín de la Vega, Spain*

Stefano Discetti

*Aerospace Engineering Research Group, Universidad Carlos III de Madrid, Leganés, Spain*

(Dated: February 24, 2022)

Reconstruction of field quantities from sparse measurements is a problem arising in a broad spectrum of applications. This task is particularly challenging when mapping between point sparse measurements and field quantities shall be performed in an unsupervised manner. Further complexity is added for moving sensors and/or random on-off status. Under such conditions, the most straightforward solution is to interpolate the scattered data onto a regular grid. However, the spatial resolution achieved with this approach is ultimately limited by the mean spacing between the sparse measurements. In this work, we propose a novel super-resolution generative adversarial network (GAN) framework to estimate field quantities from random sparse sensors without needing any full-resolution field for training. The algorithm exploits random sampling to provide incomplete views of the high-resolution underlying distributions. It is hereby referred to as RAndomly-SEEDed super-resolution GAN (RaSeedGAN). The proposed technique is tested on synthetic databases of fluid flow simulations, ocean surface temperature distributions measurements, and particle image velocimetry data of a zero-pressure-gradient turbulent boundary layer. The results show an excellent performance of the proposed methodology even in cases with a high level of gappyness ( $> 50\%$ ) or noise conditions. To our knowledge, this is the first super-resolution GANs algorithm for full-field estimation from randomly-seeded fields with no need of a full-field high-resolution representation during training nor of a library of training examples.

Sparse observations are often the only option for geophysical [1], astrophysical [2], biological [3], or fluid mechanical systems characterization [4–6]. Meteorological or oceanographic flows are remarkable examples in which atmospheric pressures, temperatures, and wind are only measured at a limited number of stations [7]; cardiac blood or flow control applications [8, 9] suffer similar issues, being sensor intrusiveness and noise contamination are particularly relevant.

Various approaches to obtain full-field description from incomplete sparsely-seeded measurements can be followed depending on the sparsity level and the number of the available samples. For limited gappyness and a sufficiently large number of samples, reconstruction techniques based on extracting flow features using methodologies such as the Proper Orthogonal Decomposition (POD) [10] or the Dynamic Mode Decomposition (DMD) [11] can be applied. For instance, the Gappy-POD filling procedures [12–14] estimate non-gappy POD modes and time coefficients by least-squares regression on the available sparse fields; the estimated modes are later used to calculate the reconstructed full fields. A recent approach, proposed in [5], merges Gappy-POD and ensemble-particle-averaging techniques, paving the way to the reconstruction of fields with significantly higher gappyness fraction. The main advantage is that a high-resolution dictionary is not required beforehand and is constructed directly using low-resolution spatially averaged fields and sparse fields. On the downside, a relatively high number of samples is required to reach suitable convergence. For cases with a limited number of samples, compressed-sensing (CS) methods provide efficient reconstruction using sparse representations [4, 9, 15]. CS is based on solving an under-determined linear system, which relates the sparse measurements with the entire fields, with additional constraints typically enforcing the smoothness of the solution [4]. A significant drawback is that they rely on a linear mapping between the sparse measurements and the high-resolution flow field. Therefore, in the cases where the relationship is strongly non-linear or when a high signal-to-noise ratio corrupts the available measurements, the use of these methods is limited to cases with relatively low gappyness fraction.

In the last years, neural network-based approaches have emerged to overcome these limitations [6, 7, 16–21]. Neural networks have been proved to be a powerful non-linear mapping tool. Super-resolution architectures based on generative adversarial networks (GANs) have been successfully applied in turbulent flows [22–25] and climate data [26] to enhance the spatial resolution and/or fill gaps between sparse measurements. While the success of these works is undeniable, they are all limited by the need for a non-sparse target for training, i.e., a library of examples where the entire field is required to train the reconstruction algorithm. This requirement often limits their applicability in real cases, in which the impossibility to record high-resolution measurements for training is more the rule than the exception.

In response to this problem, a novel super-resolution GAN framework to estimate field quantities without needing full-resolution fields for training is presented. The main advantage of the presented methodology is that it only requires the information of randomly located sensors at a variable location from sample to sample. This situation is quite common in particle-based measurements, such as tracers in particle tracking velocimetry (PTV) or phosphor thermography, but also in the case of moving sensors, such as buoys or ships. Low-resolution snapshots created by a simple binning procedure and high-resolution sparse snapshots are used for the training process, making it unnecessary to have a complete high-resolution field as the target for training. Since the proposed framework exploits the random sampling to provide incomplete views of the underlying high-resolution fields, the method is named RAndomly-SEEDed super-resolution GAN (RaSeedGAN). A set of challenging validation cases which include numerical simulations of a fluidic pinball flow, a turbulent channel flow and data from the NOAA sea surface temperature database and a zero-pressure-gradient (ZPG) turbulent boundary layer particle image velocimetry (PIV) experiment is employed to test the robustness of the methodology in complex cases where nonlinearities and noise are present.

## METHODS

Generative adversarial networks are composed of two competing networks: a generator that produces an artificial output that mimics reality, and a discriminator, which oversees distinguishing between reality and artificial outputs. For this work, the architecture proposed in [27] has been used as a baseline. The RaSeedGAN architecture is sketched in Figure 1. However, the batch-normalization layers have been removed to ensure a proper fitting of the deep layers in the architecture as proposed by [28]. In our architecture, the generator is fed with full-field information at low-resolution, directly obtained from the scattered data. Several options can be explored for this process, including interpolation, Gaussian process regression, or Voronoi tessellation, among others. In this work, we adopt a simple binning procedure. Each bin is a compact support function whose value is assigned as the average quantity measured by the sensors within it. The bin size is defined to have approximately 10 sensors per bin on average. This approach has several advantages, such as noise robustness, spatial resolution uniformity, and it generates an output similar to techniques used for field quantity estimation based on particle-image measurements, such as particle image velocimetry/thermometry. The low-resolution fields are fed to the generator, which applies a convolutional layer with filter size  $9 \times 9$  and 64 feature maps, followed by a parametric ReLU (PReLU) activation function. After these initial layers, 16 residual blocks are applied with the layout proposed by [29], i.e., a convolutional layer followed by a PReLU activation function and a second convolutional layer, with 64 feature maps of filter size  $3 \times 3$  for both convolution operations. Before increasing the resolution, a skip-connection sum is performed between the residual blocks' output and the initialization layers' output. The subpixel convolution layer proposed by [30] is used to increase the resolution. Finally, a convolution operation with linear activation function and filter size  $9 \times 9$  is applied to recover the in-plane high-resolution measurements as output.

Real and generated fields are then fed into the discriminator network. It must be noted that the real fields are sparsely sampled, thus the full-field information provided by RaSeedGAN is masked with 0s in the empty bins of the reference. The initialization of the network is carried out by a convolution operation of filter size  $3 \times 3$  and 64 feature maps, followed by the Leaky ReLU (LReLU) activation function. After this, 7 discriminator blocks of successive increasing feature maps are applied, where the discriminator blocks are composed of convolutional layers of  $3 \times 3$  size and LReLU activation function. Note that odd blocks applied a stride step larger than one to reduce the height and width of the feature maps. Finally, the feature-map tensor is flattened into a vector, followed by a fully-connected layer of 1024 neurons with LReLU activation function and output fully-connected layer with one neuron and sigmoid activation function. This output provides the probability of whether the input is real (0s) or fake (1s).

The generator loss is defined with a weighted mean-squared error of the predicted output with respect to its target. The target is built from the scattered distributions, using a binning approach similar to the proposed above. Reducing the bin size will progressively increase the probability of finding empty bins, i.e., bins without sensors. A value of 0 is set for those bins for the corresponding quantity. The error is weighted to consider only those bins in the target carrying data. Moreover, an adversarial contribution is added to the error. This adversarial loss, weighted with a factor of 0.001, is defined as the binary cross-entropy of the predicted fields, i.e., it checks whether the discriminator has labelled as 'fake' the generated fields. The discriminator loss is the mean values between the binary cross-entropy of the predicted fields and the target ones. For the latter, the error checks if the discriminator has recognized those fields as reals. All the cross-entropy errors have been perturbed with a random fluctuation of standard deviation 0.2 to increase the stability of the GAN training.

The network architectures are implemented in the open-source framework Tensorflow [31]. All models are randomly initialized. Networks' weights are updated with a learning rate of  $\epsilon = 0.0001$ . The discriminator loss function is defined as:

$$\mathcal{L}_D = -\mathbb{E}[\log D(H_R)] - \mathbb{E}[\log(1 - D(F_V \otimes G(L_R)))] \quad (1)$$

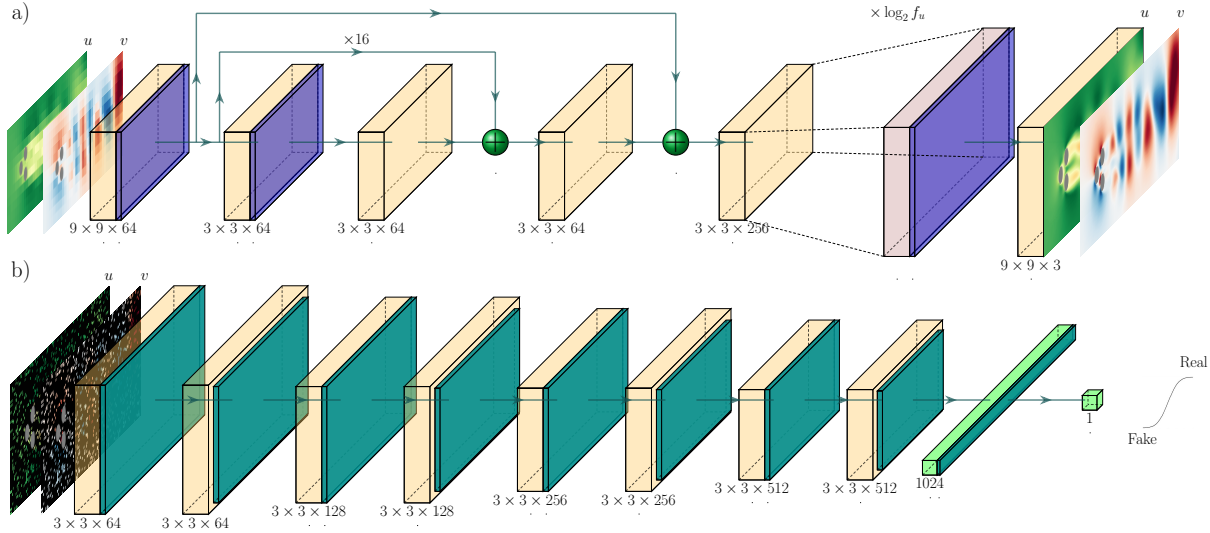


FIG. 1: Schematic illustration of RaSeedGAN architecture. a) Generator. b) Discriminator. The novel element is the use for training and testing of gappy high-resolution fields provided directly by binned scattered data.

The loss function of the generator network is defined as:

$$\mathcal{L}_G = \sum_{i=1}^{N_x} \sum_{j=1}^{N_z} |H_{R_{i,j}} - G(L_R)_{i,j}|^2 + \lambda \mathcal{L}_D, \quad (2)$$

where  $\lambda$  is a scalar parameter set to 0.001 to weigh the contribution of the adversarial loss.

The test cases included in this work have been trained during 100 epochs with 8 samples per batch. The generator and discriminator states have been stored every 5 epochs to find the optimum point before the GAN starts overfitting. The weights of both networks have been updated using Adam optimizer with a learning rate of 0.0001.

## RESULTS

In this section, the RaSeedGAN algorithm is applied on synthetic test cases generated from Direct Numerical Simulation (DNS) of fluid flows and on real experimental data. Two synthetic test cases with different challenges are considered: velocity data of the wake of a cluster of three cylinders, which has a clear shedding signature, and a turbulent channel flow at a moderate Reynolds number with an extensive scale range. Additionally, two complex experimental test cases are chosen: temperature data from the NOAA sea surface temperature and an in-house experimental zero-pressure-gradient (ZPG) turbulent boundary layer (TBL) with Particle Image Velocimetry (PIV).

### A. Test cases description

Test Case 1 consists of a *fluidic pinball* [32], a two-dimensional wake flow around a cluster of three equidistantly-spaced cylinders with equal radius  $R = D/2$ , whose centres form an equilateral triangle with a side length equal to  $3R$ . The triangle is oriented with an upstream vertex and the downstream side orthogonal to the freestream flow, located at  $x = 0$  and centred on the  $y$ -axis. The wake of the pinball includes the interaction of the wakes of three bodies, a region of development and the final merging in a large-scale shedding wake. The DNS data at  $Re_D = 130$  (referred as chaotic regime [32]) are used to generate synthetic PIV data. The details of the simulation settings and flow behaviour can be found in [32].

A set of 4737 fields with scattered vectors are generated. The first 4000 fields are used for training, while the rest is used for testing. The domain spans from  $-5D$  to  $8.04D$  in the streamwise direction and  $-3.84D$  to  $3.84D$  in the spanwise direction. In order to simulate a typical PIV setup, we discretized the domain with  $25\text{pix}/D$ , which would result in images with  $576 \times 192$  pixels. The vectors are randomly distributed to achieve an image density of 0.01 vectors per pixel, i.e. approximately 1100 vectors are generated for each sample. The low-resolution input is built setting the binning region to  $32 \times 32$  pixels with 50% overlap, corresponding on approximately 10 vectors per bin.

Beware that these parameters aim to simulate the typical processing of PIV, in which the measured velocity closely relates to the average velocity measured within the interrogation window (here referred to as bin). For this first test case, the RaSeedGAN seeks to achieve upsampling levels ranging from  $f_u = 2 - 8$ , with  $f_u$  being the upsampling factor. The window used to bin the vector fields has a size equal to  $b = D_I/f_u$ , with  $b, D_I$  being the bin size of the binned data and the bin size for the low-resolution data, respectively. Furthermore, the grid is refined by the same amount, thus maintaining the overlap between adjacent bins. It is important to remark that selecting a smaller bin increases the levels of gappyness of the distributions to be reconstructed. The level of gappyness is approximately 11%, 57%, 87% for  $f_u = 2, 4, 8$ , respectively.

Test Case 2, generated from a dataset available at the Johns Hopkins Turbulence Database (<http://turbulence.pha.jhu.edu/>), is a turbulent channel flow with a dimension of 2 half-channel-heights  $h$  from wall to wall,  $3\pi h$  in the spanwise direction and  $8\pi h$  in the streamwise direction. The details of the simulation settings and flow behaviour can be found in [33]. For our simulated experiments, sub-domains are taken of size  $2h \times h$  in the streamwise and wall-normal directions, respectively. Such domains have been discretized with  $512\text{pix}/h$  and seeded with particles with a density of 0.01 particles per pixel. The particles have been randomly distributed in the subdomain and tracked for 10 time steps of the simulations to generate the position in the second frame. A time separation of 1 convective time between snapshots is set to ensure statistical independence. In order to obtain a sufficient number of snapshots, data are extracted in subdomains at different locations in the streamwise and spanwise directions. The streamwise and spanwise separation between domains was equal to  $2h$  and  $0.25h$ , respectively. A total of 11856 snapshots have been generated, with 10000 used for training. As in the previous test case, the reference low-resolution dataset is built with a bin size of  $32 \times 32$  pixels with 50% overlap. Upsampling factors up to 8 have been tested.

In all cases, the binned distributions for training are generated using directly the original positions on the particles (or point sensors) rather than performing particle tracking on virtual images. Noise in the measurement is introduced by adding a random perturbation on velocity vectors of realistic intensity. For the pinball test case, a moderate Gaussian noise with a standard deviation of 0.01 pixels is added to the displacement vectors. For the channel, a higher noise is introduced (0.1 pixels) to account for the higher freestream displacement if compared to the pinball case. In both cases, the error realistically represents noise perturbation of Particle Tracking Velocimetry data. With this approach, we attempt to isolate the errors due to spatial resolution limitations while maintaining a controlled random error level due to uncertainty in feature matching. The gappyness level is 12%, 43%, 85% for  $f_u = 2, 4, 8$ , respectively.

The Test Case 3 is the NOAA sea surface temperature (<http://www.esrl.noaa.gov/psd/>), based on temperature data collected by satellites and ships. A total of 7305 temperature fields have been acquired, ranging from January 1<sup>st</sup> 2000 to December 21<sup>st</sup> 2019, of which 6000 have been used for training and the rest for testing. The original dataset has been interpolated on a grid with  $720 \times 1440$  points. Point temperature measurements have been extracted at approximately 10300 locations per sample and used to generate the low-resolution training dataset and the sparse high-resolution target. For the low-resolution training dataset, a bin size of  $32 \times 32$  points has been selected, resulting in approximately 10 points on average per bin. Upsampling factors of  $f_u = 2, 4, 8$  have been explored. The gappyness level correspond to 36%, 69% and 90% for upsampling factors of  $f_u = 2, 4, 8$  respectively.

Test Case 4 is an experimental dataset of a turbulent boundary layer flow in a wind tunnel with Particle Image Velocimetry. The dataset comprises 39000 images, with a spatial resolution of  $48.4\text{pix}/mm$ . The real density of identified vectors is 0.006 vector per pixel, which results in approximately 25000 vectors in an area of  $2048 \times 2048$  pixels. The flow fields have a domain size  $1.68 \times 1.68 \delta_{99}$  in the streamwise and wall-normal directions, respectively, where  $\delta_{99}$  is the boundary layer thickness. In order to have a ground truth available for comparison, the low-resolution field is estimated on a fictitiously large window of  $128 \times 128$  pixels with 50% overlap with a multi-step PIV interrogation [34]. Then an analysis using a window with  $32 \times 32$  pixels is used to generate a high-resolution reference. It must be remarked here that these high-resolution fields are not used in any form in the training process and are just exploited for performance assessment. For the sake of a fair comparison, the number of vectors is artificially reduced to only 2560 vectors per sample by randomly dropping sensors. This corresponds to 10 vectors in the original window of  $128 \times 128$  pixels, thus resulting in a mean vector spacing of 40 pixels. The sparse binned distributions for GANs training are obtained by binning with upsampling factors  $f_u = 2, 4$ , resulting in a gappyness level of 15% and 61%, respectively. Of the 39000 fields available, 30000 are used for training, while the rest are used for testing.

## B. Validation and discussion

For all validation cases, we explore the performances of RaSeedGAN with instantaneous visualisations of reconstructed fields. Figure 2 shows an instantaneous realisation for all the cases considered under study, including in columns: the input low-resolution (LR) field, the binned field, referred as “Sparse HR (high-resolution) Reference”, the reconstruction achieved with the RaSeedGAN algorithm and the reference field used to generate the particle distributions. The complete high-resolution data is included in the last column of Figure 2 as a quality check, although it is not used

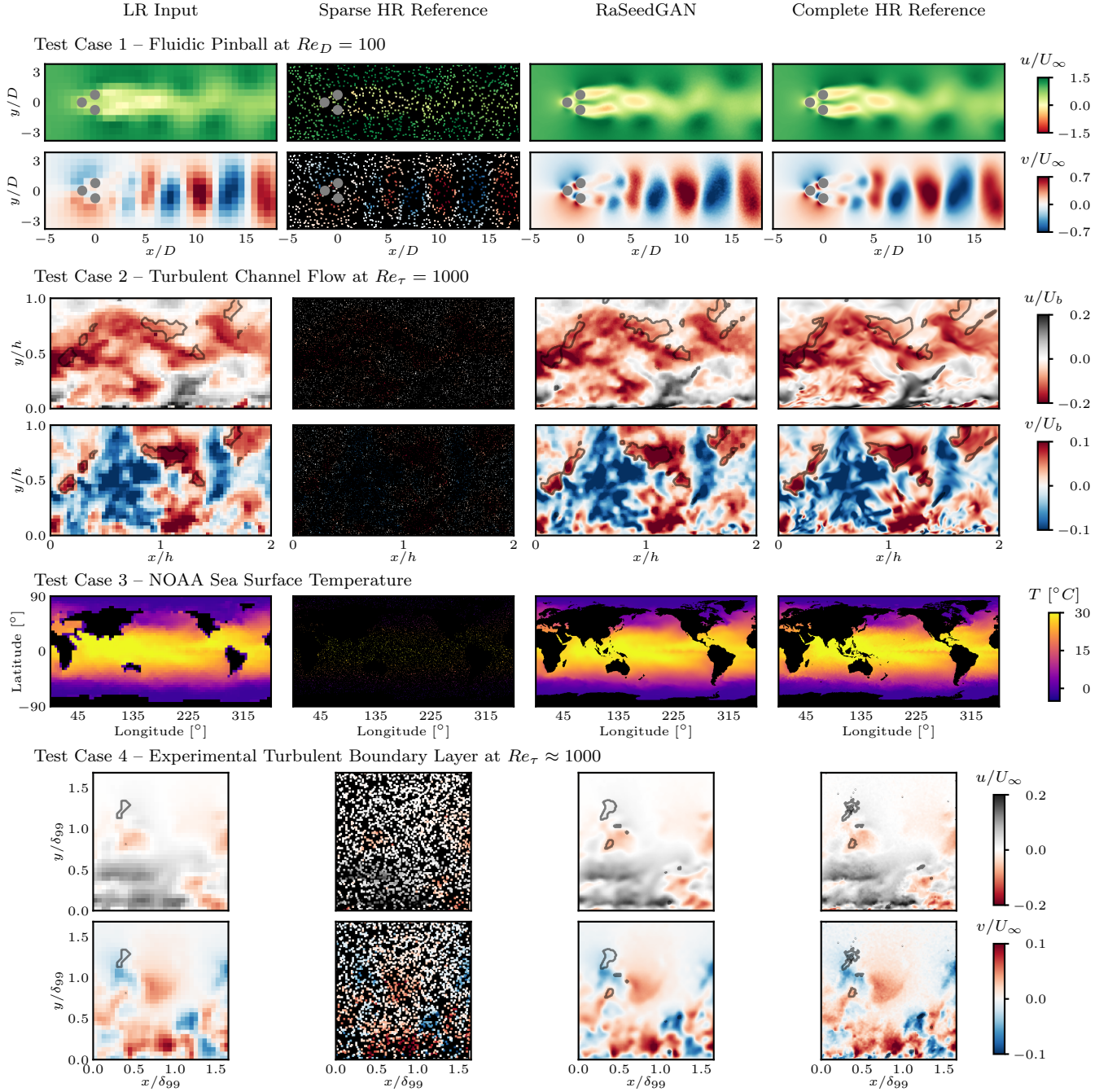


FIG. 2: Panel of applications, with examples of instantaneous field reconstructions. The columns indicate, from left to right: low-resolution input field; binned distribution, with  $f_u = 8$  for Test Case 1, 2 and 3 and  $f_u = 4$  for Test Case 4; reconstruction using the proposed sparsely-trained super-resolution GANs; the reference full field. From top to bottom: wake of the fluidic pinball from DNS, streamwise and crosswise velocity components; turbulent channel flow from DNS, wall-parallel and wall-normal velocity component; measurement of ocean surface temperature; temperature field from NOAA sea surface data; experimental data of a turbulent boundary layer, wall-parallel and wall-normal velocity components. Black isolines in Test Case 2 and 4 indicate *uvsters*.

at any moment during training. Furthermore, Table I reports the pixel-based root mean squared error for each test case and upsampling levels compared to the error obtained by a standard cubic interpolation method. The error is normalised to the standard deviation of the corresponding quantity.

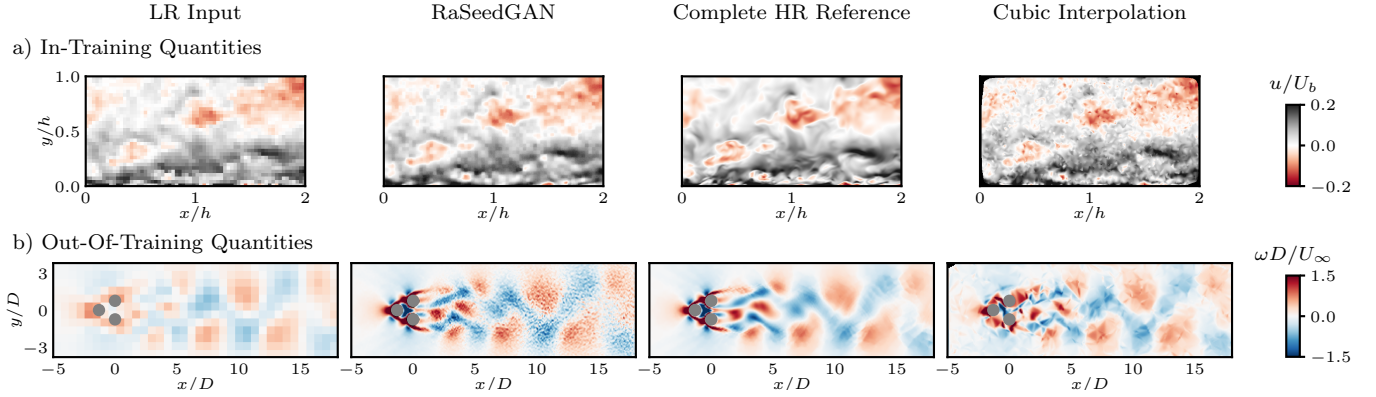


FIG. 3: Comparison of the reconstructed results with the standard cubic interpolation. a) Instantaneous wall-parallel velocity field of the turbulent channel flow from DNS. b) Out-of-plane vorticity distribution  $\omega$  for the fluidic pinball. The columns indicates from left to right: low-resolution input field (left), reconstruction using the proposed RaSeedGAN with  $f_u = 8$  (center), the reference field used to generate the test case (right) and reconstruction obtained using the standard cubic interpolation.

TABLE I: Pixel-based root mean squared error for each test case, scaled with the standard deviation of their fluctuating quantities. In parenthesis, error of reconstruction with cubic interpolation.

$f_u$	Test Case 1		Test Case 2		Test Case 3		Test Case 4	
	$u$	$v$	$u$	$v$	$T$	$u$	$v$	
2	0.304 (0.956)	0.237 (0.511)	0.274 (0.314)	0.312 (0.363)	0.718 (0.742)	0.204 (0.738)	0.275 (0.743)	
4	0.207 (1.544)	0.178 (0.720)	0.276 (0.309)	0.302 (0.351)	0.720 (1.087)	0.177 (0.642)	0.228 (0.642)	
8	0.163 (2.176)	0.149 (1.004)	0.282 (0.317)	0.312 (0.351)	0.716 (0.780)	-	-	

In the first row of Figure 2, an instantaneous flow visualisation of the fluidic pinball case with upsampling factor  $f_u = 8$  is reported for both components of the velocity fields. The RaSeedGAN allows recovering correctly the developing regions around the cylinders in the near-wake and around the cylinders. For instance, the vertical-velocity details in the front of the cylinders, which are barely seen in the low-resolution input fields, are nearly perfectly recovered. Similar performance is observed in the pinball wake, where the RaSeedGAN reconstructs the streamwise momentum defect underestimated by the low-resolution fields. The lower error level reported in Table I for cases with upsampling levels of  $f_u = 2 - 8$  supports the quality of the overall reconstructed fields. Compared to those obtained using standard cubic interpolation, the reconstruction errors are significantly lower.

Further evidence of the improved spatial resolution achieved with RaSeedGAN is provided in Figure 3, where the out-of-plane vorticity  $\omega$  is reported for  $f_u = 8$ . The same field is provided for the LR input, the complete HR reference, and cubic interpolation on a Cartesian grid of the scattered data. In this figure, the contour is labelled as “out-of-training quantities” since  $\omega$  is not used during training but is directly computed from the output data as the curl of the velocity field. The vorticity is presented in non-dimensional form using the pinball diameter  $D$  and the freestream velocity  $U_\infty$  as reference length and velocity. The low-resolution input fields are affected by significant modulation of the intensity of the vorticity peaks and attenuation of the vorticity in the shear layers near the cylinders. The proposed RaSeedGAN can recover to a large extent the main features of the vorticity distributions, including the details in the space in between the cylinders, proving that the reconstructed fields are valid to calculate secondary quantities.

In the second row of Figure 2, the streamwise and wall-normal velocity contours for the turbulent channel flow simulation are represented. Alongside this, contours that identify extreme Reynolds-shear-stress events - the so-called *uvst*ers as defined in [35] - have been plotted. The *uvst*ers, together with the clusters of vortices, play a crucial role in the modelling of the dynamics of wall-bounded turbulence based on coherent structures [35]. The recovery of wall-attached vertical velocity fluctuations in the near-wall region is remarkable, where even the recovery of small structures is appreciable. Regarding the outer part of the flow, the *uvst*ers are largely improved. Analysing the error reconstruction of Table I, the RaSeedGAN still outperforms the standard cubic interpolation, although in this case to a lower extent due to the richer range of spatial scales involved.

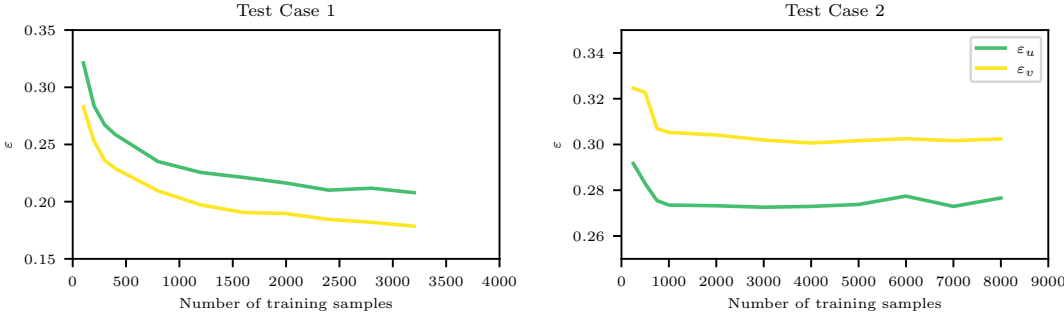


FIG. 4: Pixel-based root mean square error as a function of the number of training samples for Test Case 1 (left) and Test Case 2 (right) with  $f_u = 4$ . The error is scaled with the standard deviation of the corresponding fluctuating quantities. Green and yellow lines indicate respectively the error on the streamwise and crosswise velocity components.

In order to further assess the difference between the presented method and standard interpolation visually, Figure 3 shows a comparison of the streamwise velocity field of RaSeedGAN reconstruction against the standard cubic interpolation reconstruction (in this case labelled as “In-Training Quantities” since the streamwise velocity component is used during training). It is observed that RaSeedGAN provides a good recovery of high-resolution information without introducing noise jittering, as observed in the case of the cubic interpolation.

It must be remarked that, for both test cases, we used for training a relatively large number of samples to eliminate doubts on the training convergence. Nonetheless, the performances seem to be affected only to a small extent when working on reduced-size datasets, as observed in Figure 4. Test Case 1 involves a narrower range of scales and a less complex behaviour; this allows a continuous improvement of the error as the number of samples increases. Nonetheless, it has to be remarked that the error is substantially lower than cubic interpolation even with less than 500 training samples. On the other hand, due to the more complex behaviour of moderate-Reynolds-number channel flow, there seems to be no significant gain in increasing the number of samples beyond 1000 for Test Case 2.

In the third row of Figure 2, an instantaneous temperature field visualisation of the NOAA sea surface temperature with upsampling factor  $f_u = 8$  is reported. The RaSeedGAN allows recovering the temperature fields with a higher level of detail, as is evident from the reconstructed silhouette of the continents of the Earth. Also, in this test case, the error level reported in Table I for cases with upsampling levels of  $f_u = 2 - 8$  is lower than the obtained using standard cubic interpolation.

In the fourth row of Figure 2, the streamwise and wall-normal velocity contours for the experimental data of ZPG TBL flow are presented. As for Test Case 2, the contours that represent the *uvstres* have also been plotted. It has to be remarked that this particular case is an actual experiment in which the noisy conditions are natural and not simulated nor imposed. Again, as in the turbulent channel flow case, the recovery of wall-attached vertical velocity fluctuations in the near-wall region is observed even though the quality of the reconstruction does not match the one reported in Test Case 2. This result is not surprising since the quality of the experimental data is lower than the synthetic data. This statement is supported by the performance of the standard cubic interpolation reported in Table I, being the difference of the RaSeedGAN and the cubic interpolation more considerable than in Test Case 2.

As a further indicator of the quality of the reconstruction achieved with RaSeedGAN, the wall-normal profiles of first and second-order statistics of the streamwise velocity are reported in Figure 5a. The quantities are presented in inner scaling, i.e. the mean velocity  $U$  and the standard deviation of the fluctuation  $u'$  are scaled with the friction velocity  $u_\tau$ , while the wall-normal coordinate  $y$  is scaled with the viscous length scale  $\ell^*$ . Inner-scaled quantities are indicated with the superscript  $+$ . The results are obtained with ensemble averaging over the testing dataset and spatial averaging along the streamwise direction. For Test Case 2, the reference profiles are directly extracted from the simulation data in the Johns Hopkins Turbulence Database. For Test Case 4, the reference profile from the high-resolution PIV analysis is reported. For completeness, profiles from a friction-Reynolds-number matched simulation are also included [36]. It is important to remark that the network is not trained to recover flow statistics but rather to reconstruct field features; consequently, this assessment can be considered a fair metric for faithful flow reconstruction. Although RaSeedGAN seems to improve the turbulence statistics profiles of the initial low-resolution data, it is observed that the cubic interpolation seems to have better performances, especially in the inner region, i.e. below 15 wall units (which corresponds to about 8 pixels in Test Case 2, and 16 pixels in Test Case 4). This result, apparently at odd with the error statistics, is not surprising since it is indicative that RaSeedGAN might inherit part of

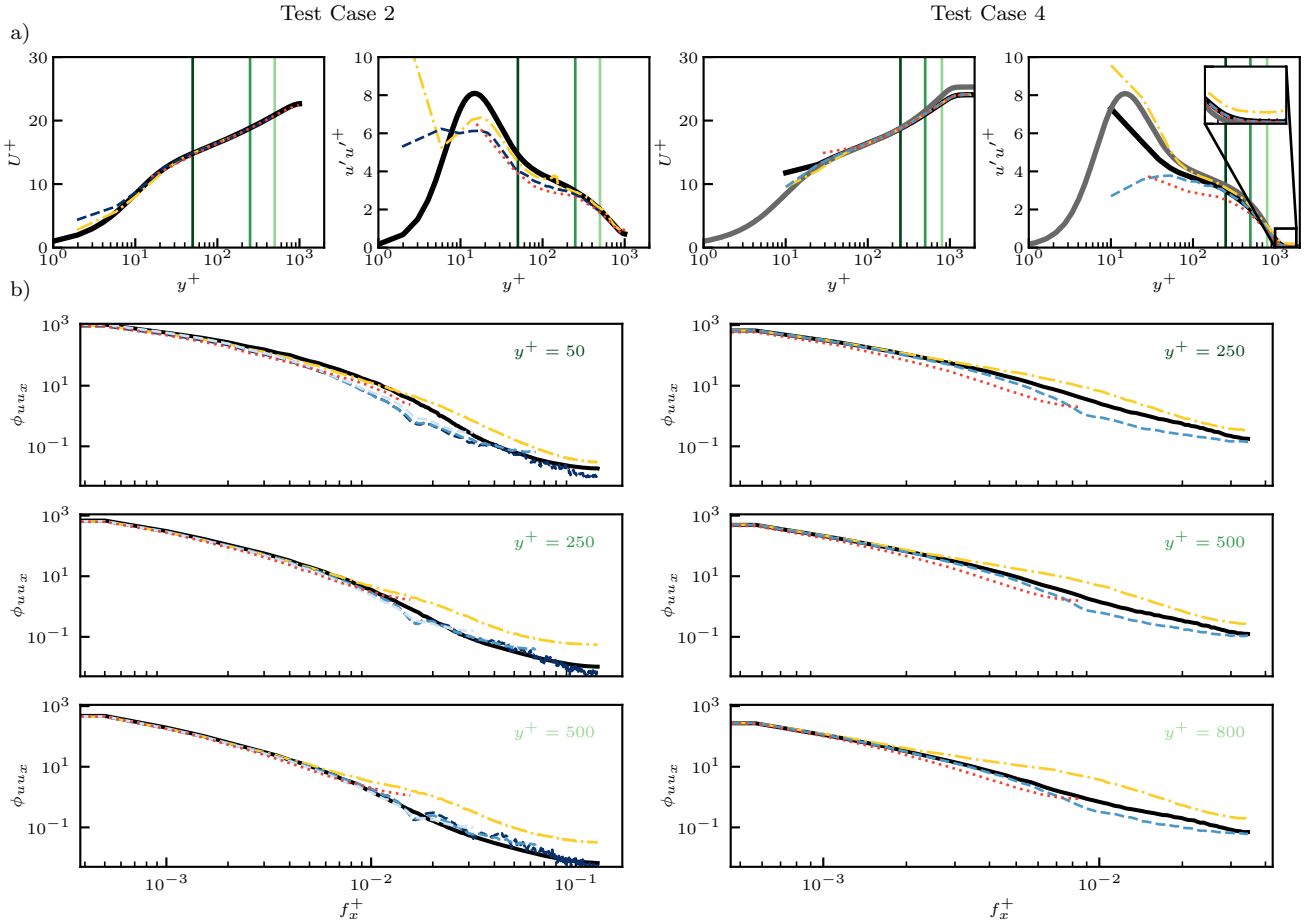


FIG. 5: a) Inner-scaled mean streamwise velocity and variance profiles for Test Case 2 (DNS turbulent channel flow) and Test Case 4 (experimental turbulent boundary layer). Lines represents the data used to calculate the quantity: high-resolution reference (solid black), low-resolution original measurements (dotted red), cubic interpolation (yellow dashed-dotted) and RaSeedGAN reconstruction (dashed blue, from light to dark indicating  $f_u = 2, 4, 8$ ). The inset in the variance profile of Test Case 4 provides a magnified view of the region with wall distance above 1000 inner units. Vertical green lines (from dark to light for increasing distance from the wall) indicate stations where the streamwise turbulent spectra are computed. For Test Case 4, gray profiles refer to data from [36]. b) Streamwise turbulent spectra at different wall distances.

the intensity modulation error from the low-resolution field, while cubic interpolation works directly on the pointwise data. On the other hand, fields obtained from cubic interpolation have visibly higher noise contamination. Thus, the variance estimation might be biased towards higher intensity due to noise, partly compensating for modulation issues and providing a misleading offset towards the reference profiles. This offset effect is well known in the fluid mechanics' community [37], and evidences of it can be observed at wall distances larger than 1000 wall-units for Test Case 4, where a plateau of the variance is observed for the cubic interpolation data to a higher value than the reference and the RaSeedGAN data (see inset of Figure 5a). To better assess the resolution in terms of scales of the flow and discern the noise contamination, the streamwise spectra of the velocity fluctuations are computed at different distances from the wall (see Figure 5b). It is observed that, except for small wall distances, RaSeedGAN can significantly increase the reach of the spectrum and follow with high fidelity the high-resolution reference. In all cases, the cubic interpolation data deliver a spectrum that peels away from the reference already at a relatively large scale. This effect can be ascribed to white-noise contamination of the estimated fields, as observed in the reconstructed field from Figure 3. If considering as cut-off the frequency at which the spectrum of the low-resolution data and RaSeedGAN reach 80% of the intensity of the reference spectrum, scales of at least 3 times smaller are recovered in all cases of Figure 5 except for  $y^+ = 50$  of Test Case 2.

## CONCLUSIONS

A novel deep-learning approach based on generative adversarial networks to perform super-resolution reconstruction of sparse measurements has been proposed and assessed. The method exploits the ability of the neural networks to learn mapping functions even when some layers have randomly-ignored neurons during the training process. We propose the RaSeedGAN method based on a GAN architecture that can obtain a non-linear mapping to high-resolution reconstructed images, using as inputs sparse low-resolution images obtained by binning the randomly-distributed sensor inputs, and as targets the original incomplete sparse measurements. RaSeedGAN allows the user great flexibility for application to experimental data in configurations where high-resolution benchmarks are not available. Its main novelty is that a full field is not required beforehand and is constructed directly using gappy binned images and the original sparse measurements. Different examples that include numerical and experimental data from velocity and temperature measurements were successfully tested, demonstrating the proposed method's accuracy and robustness even in the presence of real noisy data. We have also demonstrated that the resulting fields could calculate quantities that required a numerical derivation process with better accuracy than standard interpolation.

### Acknowledgements

This project has received funding from the European Research Council (ERC) under the European Union's Horizon 2020 research and innovation programme (grant agreement No 949085). NOAA High Resolution SST data provided by the NOAA/OAR/ESRL PSL, Boulder, Colorado, USA.

### Data availability

The datasets will be made publicly available upon publication.

### Code availability

The codes will be made publicly available upon publication.

---

[1] T. Bolton and L. Zanna, Applications of deep learning to ocean data inference and subgrid parameterization, *J. Adv. Model. Earth Sy.* **11**, 376 (2019).

[2] K. Akiyama, A. Alberdi, W. Alef, K. Asada, R. Azulay, A.-K. Baczkó, D. Ball, M. Baloković, J. Barrett, D. Bintley, *et al.*, First M87 event horizon telescope results. III. Data processing and calibration, *Astrophys. J. Lett.* **875**, L3 (2019).

[3] A. Yakhot, T. Anor, and G. E. Karniadakis, A reconstruction method for gappy and noisy arterial flow data, *IEEE T. Med. Imaging* **26**, 1681 (2007).

[4] K. Manohar, B. W. Brunton, J. N. Kutz, and S. L. Brunton, Data-driven sparse sensor placement for reconstruction: Demonstrating the benefits of exploiting known patterns, *IEEE Contr. Syst. Mag.* **38**, 63 (2018).

[5] J. Cortina-Fernández, C. Sanmiguel Vila, A. Iapiro, and S. Discetti, From sparse data to high-resolution fields: ensemble particle modes as a basis for high-resolution flow characterization, *Exp. Therm. Fluid Sci.* **120**, 110178 (2020).

[6] K. Fukami, R. Maulik, N. Ramachandra, K. Fukagata, and K. Taira, Global field reconstruction from sparse sensors with voronoi tessellation-assisted deep learning, *Nat. Mach. Intell.* **3**, 945– (2021).

[7] K. Gundersen, A. Oleynik, N. Blaser, and G. Alendal, Semi-conditional variational auto-encoder for flow reconstruction and uncertainty quantification from limited observations, *Phys. Fluids* **33**, 017119 (2021).

[8] H. Shen, X. Li, Q. Cheng, C. Zeng, G. Yang, H. Li, and L. Zhang, Missing information reconstruction of remote sensing data: A technical review, *IEEE Geosci. Remote Sens. Mag.* **3**, 61 (2015).

[9] J. L. Callaham, K. Maeda, and S. L. Brunton, Robust flow reconstruction from limited measurements via sparse representation, *Phys. Rev. Fluids* **4**, 103907 (2019).

[10] G. Berkooz, P. Holmes, and J. L. Lumley, The proper orthogonal decomposition in the analysis of turbulent flows, *Annu. Rev. Fluid Mech.* **25**, 539 (1993).

[11] P. J. Schmid, Dynamic mode decomposition of numerical and experimental data, *J. Fluid Mech.* **656**, 5 (2010).

[12] R. Everson and L. Sirovich, Karhunen–Loeve procedure for gappy data, *JOSA A* **12**, 1657 (1995).

[13] D. Venturi and G. E. Karniadakis, Gappy data and reconstruction procedures for flow past a cylinder, *J. Fluid Mech.* **519**, 315 (2004).

[14] S. G. Raben, J. J. Charonko, and P. P. Vlachos, Adaptive gappy proper orthogonal decomposition for particle image velocimetry data reconstruction, *Meas. Sci. Technol.* **23**, 025303 (2012).

[15] X. Huang, Compressive sensing and reconstruction in measurements with an aerospace application, *AIAA J.* **51**, 1011 (2013).

- [16] R. Maulik, K. Fukami, N. Ramachandra, K. Fukagata, and K. Taira, Probabilistic neural networks for fluid flow surrogate modeling and data recovery, *Phys. Rev. Fluids* **5**, 104401 (2020).
- [17] H. Gao, L. Sun, and J.-X. Wang, Super-resolution and denoising of fluid flow using physics-informed convolutional neural networks without high-resolution labels, *Phys. Fluids* **33**, 073603 (2021).
- [18] N. B. Erichson, L. Mathelin, Z. Yao, S. L. Brunton, M. W. Mahoney, and J. N. Kutz, Shallow neural networks for fluid flow reconstruction with limited sensors, *Proc. Roy. Soc. A* **476**, 20200097 (2020).
- [19] L. Sun and J.-X. Wang, Physics-constrained bayesian neural network for fluid flow reconstruction with sparse and noisy data, *Theor. Appl. Mech. Lett.* **10**, 161 (2020).
- [20] A. Arzani, J.-X. Wang, and R. M. D’Souza, Uncovering near-wall blood flow from sparse data with physics-informed neural networks, *Phys. Fluids* **33**, 071905 (2021).
- [21] S. L. Brunton, B. R. Noack, and P. Koumoutsakos, Machine learning for fluid mechanics, *Annu. Rev. Fluid Mech.* **52**, 477 (2020).
- [22] K. Fukami, K. Fukagata, and K. Taira, Super-resolution reconstruction of turbulent flows with machine learning, *J. Fluid Mech.* **870**, 106 (2019).
- [23] H. Kim, J. Kim, S. Won, and C. Lee, Unsupervised deep learning for super-resolution reconstruction of turbulence, *J. Fluid Mech.* **910** (2021).
- [24] A. Güemes, S. Discetti, A. Ianiro, B. Sirmacek, H. Azizpour, and R. Vinuesa, From coarse wall measurements to turbulent velocity fields through deep learning, *Phys. Fluids* **33**, 075121 (2021).
- [25] Z. Deng, C. He, Y. Liu, and K. C. Kim, Super-resolution reconstruction of turbulent velocity fields using a generative adversarial network-based artificial intelligence framework, *Phys. Fluids* **31**, 125111 (2019).
- [26] K. Stengel, A. Glaws, D. Hettinger, and R. N. King, Adversarial super-resolution of climatological wind and solar data, *Proc. Natl Acad. Sci.* **117**, 16805 (2020).
- [27] C. Ledig, L. Theis, F. Huszár, J. Caballero, A. Cunningham, A. Acosta, A. Aitken, A. Tejani, J. Totz, Z. Wang, *et al.*, Photo-realistic single image super-resolution using a generative adversarial network, in *Proc. IEEE CVPR* (2017) pp. 4681–4690.
- [28] X. Wang, K. Yu, S. Wu, J. Gu, Y. Liu, C. Dong, Y. Qiao, and C. C. Loy, ESRGAN: Enhanced Super-Resolution Generative Adversarial Networks, in *Proc. Eur. Conf. Comput. Vis. Workshop* (2018), edited by L. Leal-Taixé and S. Roth (2018) pp. 63–79.
- [29] S. Gross and M. Wilber, Training and investigating residual nets, *Facebook AI Research* **6**, 3 (2016).
- [30] W. Shi, J. Caballero, F. Huszár, J. Totz, A. P. Aitken, R. Bishop, D. Rueckert, and Z. Wang, Real-time single image and video super-resolution using an efficient sub-pixel convolutional neural network, in *Proc. IEEE CVPR* (2016) pp. 1874–1883.
- [31] M. Abadi, P. Barham, J. Chen, Z. Chen, A. Davis, J. Dean, M. Devin, S. Ghemawat, G. Irving, M. Isard, *et al.*, Tensorflow: A system for large-scale machine learning, in *12th USENIX symposium on operating systems design and implementation (OSDI 16)* (2016) pp. 265–283.
- [32] N. Deng, B. R. Noack, M. Morzyński, and L. R. Pastur, Low-order model for successive bifurcations of the fluidic pinball, *J. Fluid Mech.* **884**, A37 (2020).
- [33] Y. Li, E. Perlman, M. Wan, Y. Yang, C. Meneveau, R. Burns, S. Chen, A. Szalay, and G. Eyink, A public turbulence database cluster and applications to study lagrangian evolution of velocity increments in turbulence, *J. Turbul.* **9**, N31 (2008).
- [34] F. Scarano, Iterative image deformation methods in PIV, *Meas. Sci. Technol.* **13**, R1 (2001).
- [35] A. Lozano-Durán, O. Flores, and J. Jiménez, The three-dimensional structure of momentum transfer in turbulent channels, *J. Fluid Mech.* **694**, 100 (2012).
- [36] P. Schlatter and R. Örlü, Assessment of direct numerical simulation data of turbulent boundary layers, *J. Fluid Mech.* **659**, 116 (2010).
- [37] C. Atkinson, N. A. Buchmann, O. Amili, and J. Soria, On the appropriate filtering of PIV measurements of turbulent shear flows, *Exp. Fluids* **55**, 1 (2014).

## I. Credit author statement

AG: Methodology, Software, Validation, Investigation, Data Curation, Writing - Original Draft, Writing - Review & Editing, Visualization. CSV: Conceptualization, Methodology, Writing - Original Draft, Writing - Review & Editing. SD: Methodology, Software, Resources, Data Curation, Supervision, Writing - Original Draft, Writing - Review & Editing, Funding acquisition

## II. Declaration of interest

The authors report no conflict of interest.